Supercontinuum emission and enhanced self-guiding of infrared femtosecond filaments sustained by third-harmonic generation in air

L. Bergé,[1,*] S. Skupin,[1,2] G. Méjean,[3] J. Kasparian,[3] J. Yu,[3] S. Frey,[3] E. Salmon,[3] and J. P. Wolf[3]
[1]*Département de Physique Théorique et Appliquée, CEA/DAM Ile de France, Boîte Postale 12, 91680 Bruyères-le-Châtel, France*
[2]*Institute for Condensed Matter Theory and Solid State Optics, Friedrich-Schiller-Universität Jena, Max-Wien-Platz 1, 07743 Jena, Germany*
[3]*Laboratoire de Spectrométrie Ionique et Moléculaire, Université Claude Bernard Lyon 1, UMR-CNRS 5579, F-69622 Villeurbanne cedex, Lyon, France*
(Received 15 July 2004; published 5 January 2005)

The long-range propagation of two-colored femtosecond filaments produced by an infrared (IR) ultrashort pulse exciting third harmonics (TH) in the atmosphere is investigated, both theoretically and experimentally. First, it is shown that the coupling between the pump and TH components is responsible for a wide spectral broadening, extending from ultraviolet (UV) wavelengths (220 nm) to the mid-IR (4.5 μm). Supercontinuum generation takes place continuously as the laser beam propagates, while TH emission occurs with a conversion efficiency as high as 0.5%. Second, the TH pulse is proven to stabilize the IR filament like a saturable quintic nonlinearity through four-wave mixing and cross-phase modulation. Third, the filamentation is accompanied by a conical emission of the beam, which becomes enlarged at UV wavelengths. These properties are revealed by numerical simulations and direct experimental observations performed from the Teramobile laser facility.

DOI: 10.1103/PhysRevE.71.016602 PACS number(s): 42.65.Tg, 52.38.Hb, 42.65.Jx, 42.68.Ay

I. INTRODUCTION

Femtosecond laser pulses are well known to propagate over several Rayleigh lengths as robust filamentary channels in the atmosphere [1–3]. The basic principle of this self-guiding relies on a delicate balance between the nonlinear Kerr response of air, which focuses the beam and produces optical intensities as high as 10^{14} W/cm^2, and the defocusing action of ionization of air molecules, which arrests the beam collapse and excites a tenuous plasma with electron densities limited to 10^{16}–10^{17} cm^{-3}. Apart from this principle, additional mechanisms, such as higher-order terms in the nonlinear index of refraction, have been proposed as stabilizers for femtosecond filaments, not only in the atmosphere [4,5], but also in various transparent media [6]. Plasma defocusing creates ring structures in the pulse spatial profile and damps the latest time slices in the temporal profiles. Because of this complexity, several scenarios have been elaborated to explain the nature of the filamentation process, such as the self-channeling model [1,2,7], the moving focus picture [8], and the spatial replenishment [9]. Recently [10], it was proposed that the complex dynamics of filamentation could mainly be inferred from the latter scenario, the former ones clearing up intermediate stages in the filament formation according to the input beam power.

This filament process has been put in evidence both for near IR [1–3] and UV wavelengths [11–13]. In the IR domain (800 nm), femtosecond pulses were shown to undergo a strong spectral broadening caused by the following: In the early propagation, the pulse is subject to self-phase modulation (SPM) in regimes for which Kerr compression (self-focusing) dominates, starting with beam powers (P_{in}) well above the critical power for self-focusing (P_{cr}). SPM symmetrically increases the pulse spectrum to some extent, until plasma generation comes into play. Self-induced ionization then depletes the back of the pulse and keeps untouched its leading edge, which creates a redshift in the pulse spectrum [14,15]. This redshift has also been observed in dielectrics such as fused silica or sapphire samples [16,17]. It was explained by the same cause, namely, the occurrence of a steep leading edge in the pulse temporal profile (see, e.g., Agrawal [18]). According to the number of critical powers in the initial beam, femtosecond pulses can undergo distinct sequences of focusing/defocusing events, triggered by the refocusing time slices (back or front) raising in the pulse. Such sequences favor multipeaked temporal profiles which participate in enlarging more and more the spectra. In addition to these distortions, there exists a significant broadening of the angular spectrum dictated by the spatial variations of the pulse phase. These variations are responsible for conical emission (CE) [2,19] through which the beam diverges as a concentric rainbow with colors ranging from red to green.

These two effects, i.e., spectral broadening and CE, constitute the key tools currently used for atmospheric remote sensing by ultrashort laser pulses [20–26]. Temporal variations in the pulse profile indeed induce a very broad spectral continuum, spanning from the UV (350 nm) to the mid-IR ($\sim$4.5 μm) [20], so that the broadened laser beam is often termed as "white-light laser" [21,22]. Long-distance nonlinear propagation of terawatt (TW) laser pulses was found to significantly enhance such a supercontinuum generation. Filamentation could be observed up to 2 km altitudes via a detailed analysis of the conical emission. Compared with laboratory experiments limited to meter scales, the spectrum intensity was found to be enhanced up to two orders of magnitude in the IR domain [26]. This enabled the improvement of Lidar (light detection and ranging) performances through

*Electronic address: luc.berge@cea.fr

white-light emission, as many important pollutants cover large absorption bands [27].

So far, investigations on the self-channeling of femtosecond pulses have mostly concerned the central component of infrared beams (800 nm). Only recently [29,30] has the question of the coupling between this IR component and self-induced third-harmonic generation (THG) been raised. While THG is nowadays a well-known mechanism [18,31], less attention has been paid to its implications in the propagation of ultrashort laser pulses in the atmosphere. Among the references available in the literature, we can mention the works [32–35], where there has been considerable interest in high harmonic generation using intense femtosecond laser pulses focused into gases. In [32], a conversion efficiency as high as 0.1% was reported for THG in air. Higher conversion efficiency, up to 0.2%, was measured in [29,30] and the coupling of TH with the pump IR beam was shown to produce a "two-colored" femtosecond filament.

The former pioneering references, however, were limited to propagation distances never exceeding a few tens of cm and using tightly focused beams. It is thus worthwhile studying THG in the framework of long-distance propagation, involving the development of femtosecond filaments over several meters and beyond. In this respect, several points deserve to be addressed, such as determining the spectral broadening promoted by THG, understanding the influence of the third harmonics onto the self-channeling characteristics, and the incidence of THG on the conical emission.

In the present work, we numerically and experimentally investigate third-harmonic generation in air and its incidence on the filamentation of femtosecond pulses over several meters. We report a new phenomenon: The supercontinuum generation at UV-visible wavelengths produced by infrared ultrashort laser pulses in air. Implications of this UV continuous emission are very important for white-light Lidar experiments [27], as numerous atmospheric pollutants (NOx, SO_2, O_3, benzene, toluene, xylene, PAHs, formaldehyde, Hg, etc.) have strong specific UV absorption bands. Aerosol fluorescence is also excited in this region (e.g., for bioaerosol detection using amino acids as tracers [28]).

The paper is organized as follows. The model equations are first derived (Sec. II). Emphasis is then given on the superbroadband continuum in the UV-visible domain of wavelengths admitting a cutoff as low as 230 nm and an IR tail as far as 4.5 μm. By means of numerical simulations, long-distance propagation is shown to lead to a smooth continuous UV-IR broadening. This phenomenon is explained in terms of SPM of the pump wave being amplified by the TH pulse, which is locked at the constant π phase shift with the fundamental (Sec. III). Effects of THG on conical emission are also discussed (Sec. IV). Both this spectacular broadening and conical emission are experimentally reported from direct measurements and analysis of the white-light laser formed by cm-waisted pulses delivered by the Teramobile system [23] (Sec. V). An important consequence of THG is moreover the stabilization of the two-colored femtosecond filament, whose length is shown to be increased by almost one meter (Sec. VI). Long-distance propagation allows the beam to preserve part of its energy by converting the pump wave into TH with an efficiency as high as 0.5%. With a large wave-vector mismatch ($\sim 5\ \mathrm{cm}^{-1}$), harmonic generation acts on the pump field as a quintic saturation nonlinearity. Implications of these new results on the current modeling of fs pulses in air are finally discussed (Sec. VII).

II. MODEL EQUATIONS FOR ATMOSPHERIC THG BY FEMTOSECOND IR PULSES

The derivation of equations describing third-harmonic generation (THG) from an infrared pump follows the classical steps when deducing nonlinear Schrödinger (NLS) wave equations for different optical components [18]. With the ansatz

$$E \to \mathcal{E}_\omega e^{i[k(\omega)z-\omega t]} + \tilde{\mathcal{E}}_{3\omega} e^{i[k(3\omega)z-3\omega t]} \tag{1}$$

for the complex field, we get two equations for the slowly varying envelopes $\mathcal{E}_\omega$ and $\tilde{\mathcal{E}}_{3\omega}$. These equations are coupled via cross-phase modulation (XPM) and four-wave mixing (FWM) due to the cubic nonlinearity. Further on, we substitute $\tilde{\mathcal{E}}_{3\omega} \to \mathcal{E}_{3\omega} e^{i\Delta kz}$, taking into account the linear wave-vector mismatch parameter $\Delta k = 3k(\omega) - k(3\omega)$. After transforming to a reference frame moving with the group-velocity $v_g(\omega)$ of the pump wave, our propagation equations for THG in air read

$$\left(i\partial_z + \frac{1}{2k_0}\nabla_\perp^2 - \frac{k''_\omega}{2}\partial_t^2\right)\mathcal{E}_\omega + k_0 n_2 [R(t)\mathcal{E}_\omega + 2|\mathcal{E}_{3\omega}|^2\mathcal{E}_\omega + \mathcal{E}_\omega^{*2}\mathcal{E}_{3\omega}] - \left[\left(\frac{k_0}{2\rho_c} - i\frac{\sigma_\omega}{2}\right)\rho - i\frac{\beta_\omega^{(K_\omega)}}{2}|\mathcal{E}_\omega|^{2K_\omega - 2}\right]\mathcal{E}_\omega = 0, \tag{2}$$

$$\left(i\partial_z + i\Delta v^{-1}\partial_t + \frac{1}{6k_0}\nabla_\perp^2 - \frac{k''_{3\omega}}{2}\partial_t^2 - \Delta k\right)\mathcal{E}_{3\omega} + 3k_0[n_2^{3\omega}|\mathcal{E}_{3\omega}|^2\mathcal{E}_{3\omega} + 2n_2|\mathcal{E}_\omega|^2\mathcal{E}_{3\omega} + n_2\mathcal{E}_\omega^3/3] - \left[\left(\frac{k_0}{6\rho_c} - i\frac{\sigma_{3\omega}}{2}\right)\rho - i\frac{\beta_{3\omega}^{(K_{3\omega})}}{2}|\mathcal{E}_{3\omega}|^{2K_{3\omega}-2}\right]\mathcal{E}_{3\omega} = 0, \tag{3}$$

$$R(t) = \tfrac{1}{2}|\mathcal{E}_\omega|^2 + \tfrac{1}{2}\tau_K^{-1}\int_{-\infty}^{t} e^{-(t-t')/\tau_K}|\mathcal{E}_\omega(t')|^2 dt'. \tag{4}$$

The physical parameters are defined by $k_0 = 2\pi/\lambda_0 = \omega_c$, $\Delta k = -5\ \mathrm{cm}^{-1}$, while $k''_\omega = 0.2\ \mathrm{fs}^2/\mathrm{cm}$ and $k''_{3\omega} = 1\ \mathrm{fs}^2/\mathrm{cm}$ are the coefficients for normal group-velocity dispersion (GVD). $\Delta v = [v_g(3\omega)^{-1} - v_g(\omega)^{-1}]^{-1} = 0.44\ \mathrm{cm/fs}$ is the group-velocity mismatch responsible for temporal walk-off. The terms induced by the coupling between the two components involve self- and cross-phase modulations together with the FWM, allowing energy transfer between fundamental and TH fields. Here, $n_2 = 4\times 10^{-19}\ \mathrm{cm}^2/\mathrm{W}$ denotes the nonlinear Kerr index for the IR component, while $n_2^{3\omega} = 8\times 10^{-19}\ \mathrm{cm}^2/\mathrm{W}$ is that experienced by TH. The IR Kerr response of air, defined by Eq. (4), is composed of an instantaneous contribution and a delayed part with a relaxation

time $\tau_K = 70$ fs [12,14,36]. The free electron density ρ increases in time as

$$\partial_t \rho = \sum_{j=\omega,3\omega} (\rho_{\rm nt} - \rho)\sigma_{(K_j)}|\mathcal{E}_j|^{2K_j} + (\sigma_j/U_i)\rho|\mathcal{E}_j|^2, \qquad (5)$$

where the index j refers to ω and 3ω components, respectively. In Eq. (5), K_j and $\sigma_{(K_j)}$ denote the number of photons for IR (800 nm, $K_\omega = 8$) and UV wavelengths (266 nm, $K_{3\omega} = 3$), and their respective multiphoton ionization (MPI) rates $\sigma_{(8)} = 2.88 \times 10^{-99}$ s^{-1} cm^{16}/W^8, $\sigma_{(3)} = 1.91 \times 10^{-28}$ s^{-1} cm^6/W^3 [13]. Plasma response has been completed by inclusion of avalanche ionization with the inverse bremsstrahlung cross sections $\sigma_\omega = 5.44 \times 10^{-20}$ cm^2 and $\sigma_{3\omega} = 6.044 \times 10^{-21}$ cm^2. Only oxygen ionization with gap potential $U_i = 12.1$ eV is considered for a neutral medium with density $\rho_{\rm nt} = 5.4 \times 10^{18}$ cm^{-3}; $\rho_c = 1.8 \times 10^{21}$ cm^{-3} is the plasma critical density defined at 800 nm. Because avalanche ionization is weak for pulse duration <1 ps, MPI is the principal actor in generating an electron plasma. Multiphoton absorption (MPA) intervenes through the coefficients $\beta_j^{(K_j)} = \hbar\omega_j K_j \rho_{\rm nt}\sigma_{(K_j)}$, yielding $\beta_\omega^{(8)} = 3.1 \times 10^{-98}$ cm^{13}/W^7 and $\beta_{3\omega}^{(3)} = 2.31 \times 10^{-27}$ cm^3/W^2.

This system of equations resembles that proposed by Aközbek *et al.* in [29], apart from the following points: First, plasma generation by avalanche and related absorption have been included. Second, in the equation for the IR pump, the Raman-delayed Kerr response [14,36] has been taken into account. We assumed a zero delayed response for the UV component, as chosen in [13,29]. Third, MPI and MPA for the TH component have been tuned on their appropriate cross sections $(K_{(3)}, \sigma_{(3)}, \beta_{3\omega}^{(3)})$, while SPM, XPM, and FWM contributions in Eq. (3) possess different nonlinear Kerr indices.

These changes are, however, minor and preliminary simulations using the pulse parameters of Ref. [29] restored a propagation dynamics close to that commented on in this reference. In addition, we verified that simulations performed with halved nonlinear coefficients for XPM and FWM, and involving also $R(t)$ in the 3ω component, led to results comparable with the coming ones.

III. METER-RANGE PROPAGATION OF FUNDAMENTAL AND TH PULSES IN PARALLEL GEOMETRY

Equations (2)–(5) are numerically integrated by means of a parallel radial code for pulses propagating in collimated geometry, in order to produce femtosecond filaments keeping a quasiconstant diameter over several meters. Two input beam configurations are investigated: (a) Sub-mm pulses ($w_0 = 0.5$ mm) conveying a ratio of input power over critical $P_{\rm in}/P_{\rm cr} = 4$ and (b) broader beams with waist $w_0 = 0.25$ cm containing 50 critical powers. The critical power for self-focusing is defined by $P_{\rm cr} = \lambda_0^2/2\pi n_2$ and it takes the value $P_{\rm cr} = 2.55$ GW at $\lambda_0 = 800$ nm.

A. Femtosecond pulses with moderate powers

To start with, we first solve Eqs. (2)–(5) for an input pulse having a Gaussian shape

$$\mathcal{E}_\omega(z=0,r,t) = \sqrt{\frac{2P_{\rm in}}{\pi w_0^2}} e^{-r^2/w_0^2 - t^2/t_p^2}, \qquad (6)$$

with power $P_{\rm in} = 4P_{\rm cr}$, waist $w_0 = 0.5$ mm, and temporal half-width $t_p \simeq 127$ fs [≡full width at half maximum (FWHM) duration/$\sqrt{2\ln 2}$]. The beam is launched into the atmosphere in a collimated way (no focusing lens). At $z = 0$, there is no third-harmonic component ($\mathcal{E}_{3\omega} = 0$). Figure 1 summarizes the results of the numerical simulations. Figures 1(a) and 1(b) show the peak intensities of the fundamental (ω) and TH (3ω) pulses. Figures 1(c) and 1(d) represent the on-axis fluence distribution $[\mathcal{F} = \int_{-\infty}^{+\infty}(|\mathcal{E}_\omega|^2 + |\mathcal{E}_{3\omega}|^2)(r=0,z,t)dt]$ and the mean radius of the two-colored filament taken as the FWHM of the fluence, respectively. Figures 1(e) and 1(f) illustrate the maximum plasma density ($\max_t \rho$) excited by ionization of air molecules and the energy loss upon the propagation axis, computed throughout the entire simulation box. All dashed curves refer to the same quantities plotted for an IR pulse only, i.e., while maintaining $\mathcal{E}_{3\omega} = 0$ along the z axis.

From these figures, a couple of important features can already be emphasized.

(i) The ratio of peak intensities $I_\omega/I_{3\omega}$ ($I_j \equiv |\mathcal{E}_j|^2; j = \omega, 3\omega$) mostly remains $\geqslant 50$. This observation can be explained by the large phase mismatch Δk between the pump and TH components: The characteristic coherence length $L_c = \pi/|\Delta k| \approx 0.63$ cm is rather small, so the evolution of the TH peak intensity almost follows that of the fundamental. Generated TH field experiences down-conversion after a short propagation length <1 cm, which significantly limits the growth of its intensity over larger distances.

(ii) There is a noticeable enlargement of the filament range in the presence of THG: Self-guiding is enhanced by a multiplicative factor of ~ 1.5 compared with the case where TH is omitted. Note the smoother decrease in energy when both IR and UV components couple, which allows the filament to survive over longer distances and stay clamped with a longer plasma channel reaching a peak electron density $\sim 10^{16} - 10^{17}$ cm^{-3}.

In order to get a deeper insight into the nonlinear dynamics of the two-colored filament, we display in Fig. 2 information related to the on-axis temporal distortions undergone by the two components [Figs. 2(a) and 2(b)] and by an IR pulse only [Fig. 2(c)]. Here, the red zones correspond to intensity levels 60 TW/cm$^2 \leqslant I_{\max} \leqslant 80$ TW/cm^2, while yellow and green zones correspond to lower ones, i.e., 40 TW/cm$^2 \leqslant I_{\max} < 60$ TW/cm^2. Some temporal profiles are illustrated in Fig. 2(d) at different propagation distances. Figure 2(e) supplies information about the dephasing $\Delta\phi = 3\phi_\omega - \phi_{3\omega}$ between the components at two different instants, namely, $t = 0$ and $t = t_{\max}$ when the pulse intensity is maximum. Figure 2(f) finally shows the energy conversion efficiency between the fundamental and the TH pulses, inside a contour of 300 μm in diameter around the filament core (dashed line) and over the whole simulation box (solid line). This conversion efficiency is defined by the ratio between the energy in the TH component and the energy of both components. It attains values as high as 0.5% over 5 m of propagation.

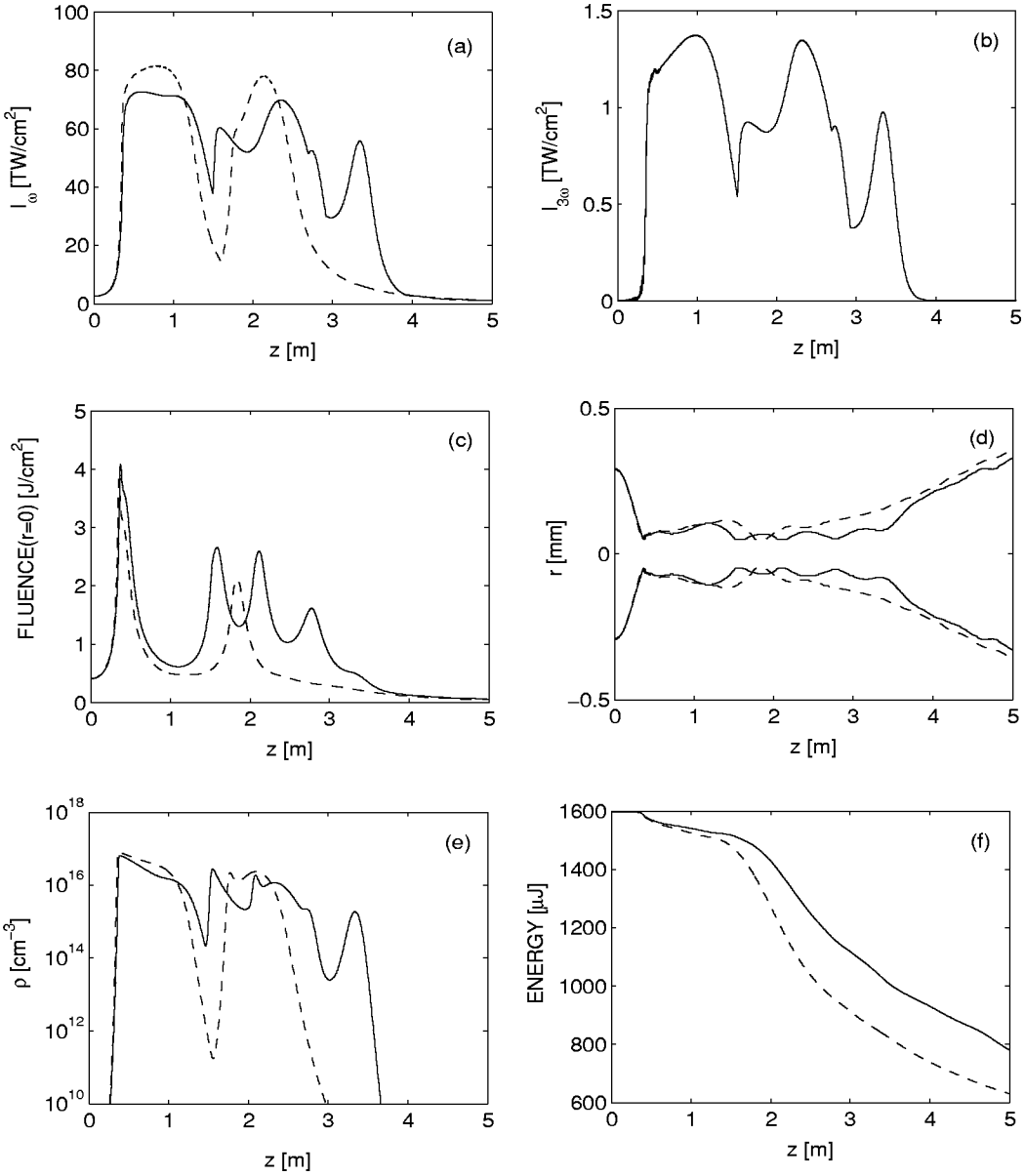

FIG. 1. (a) Peak intensities for the fundamental and (b) TH components, (c) fluence distribution, (d) mean radius (FWHM of the fluence distribution), (e) peak electron density, and (f) energy losses for a Gaussian pulse with $P_{\mathrm{in}}=4P_{\mathrm{cr}}$. Dashed lines represent the same quantities without THG.

Again we may underline important points revealed by these computations.

(iii) Temporal walk-off, which should promote the displacement of the TH component to positive times compared with the fundamental pulse profile, is negligible. The walk-off length, $L_{\Delta v}\approx 66$ cm, is about 100 times higher than the coherence length $L_c\approx 0.63$ cm, so the TH component is located at the instants when the pump field develops.

(iv) Following the "spatial replenishment dynamics" model [9], when a single component propagates, plasma generation defocuses the back of the pulse and thereby forms a leading edge ($t<0$). Afterwards, plasma partly turns off and provokes the refocusing of the trailing edge ($t>0$). This standard scenario is refound in Fig. 2(c). Note that the trail is here directed to $t=0$ at $z\simeq 2.5$ m. We attribute this reconfinement to center to the Raman-delayed Kerr response, which smooths the back of the pulse and lowers the number of peaks arising at positive times [37]. When both IR and UV components couple, we rediscover this temporal evolution, up to ~ 2 m only. Next, the dynamics changes: Temporal fluctuations develop in the pulse profile at $z\sim 2.2$ m. Two new cycles of focusing/defocusing events occur, connected with the oscillations seen in Fig. 1(c). These new events go on feeding the interplay between the leading and trailing edges in the pulse, before only one temporal peak is confined around $t=0$ at the distance $z=3.24$ m. When the pulse temporal profile relaxes to a single peak, it exhibits a typical duration $\lesssim t_p/10$.

(v) The phase difference is quasiconstant and keeps the value $\Delta\phi\simeq\pi$ almost all along the self-guiding range, up to

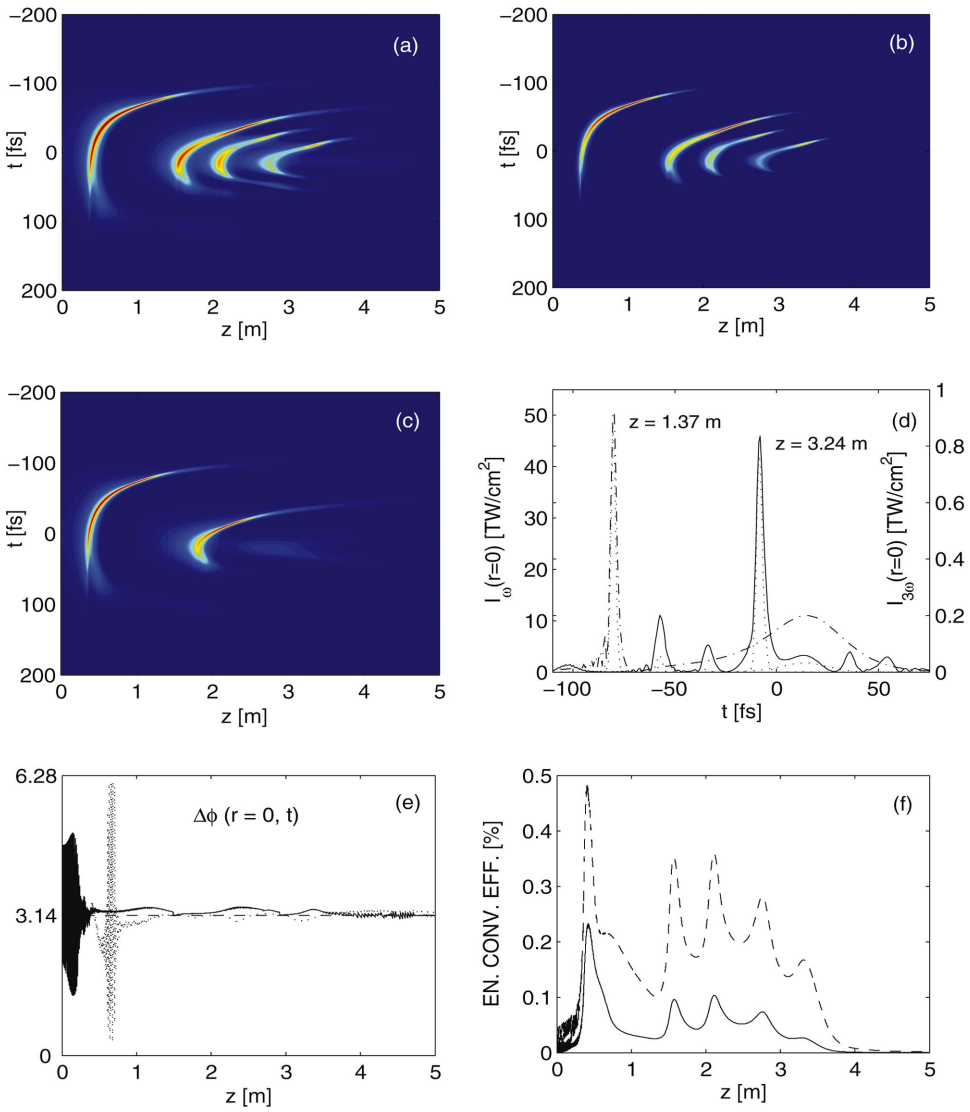

FIG. 2. (Color) Image plots of the temporal distributions for $4P_{cr}$ mm-waisted pulses: (a) fundamental pulse; (b) TH pulse; (c) IR component alone; (d) temporal profiles from the coupling between both components at $z=1.37$ m and $z=3.24$ m (TH intensity must be read on the right-hand side axis); (e) dephasing $\Delta\phi$ at $t=t_{max}$ (solid line) and $t=0$ (dashed line); (f) energy conversion efficiency around the filament core (dashed curve) and over the entire simulation box (solid curve).

few intervals in z. This property, first discovered in [29] upon a few cm only, is hence confirmed for collimated beams propagating over meter-range distances.

To understand this latter point, we may follow the procedure proposed in [29]. We decompose the pump and TH fields in phase and amplitude ($\mathcal{E}_j=A_j e^{i\phi_j}$, $j=\omega,3\omega$). Discarding transverse diffraction, walk-off, and GVD in regimes mainly driven by the nonlinearities that involve relatively weak losses [see Fig. 1(f)], we find

$$\partial_z \phi_\omega \approx -\frac{k_0\rho}{2\rho_c} + k_0 n_2 [R(t) + 2A_{3\omega}^2 + A_\omega A_{3\omega}\cos(\Delta\phi)], \quad (7)$$

$$\partial_z \phi_{3\omega} \approx -\Delta k - \frac{k_0\rho}{6\rho_c} + 3k_0 n_2^{3\omega} A_{3\omega}^2 + 3k_0 n_2 \times\left(2A_\omega^2 + \frac{A_\omega^3}{3A_{3\omega}}\cos(\Delta\phi)\right), \quad (8)$$

$$\tfrac{1}{2}\partial_z A_\omega^2 \simeq k_0 n_2 A_\omega^3 A_{3\omega}\sin(\Delta\phi), \quad (9)$$

$$\tfrac{1}{2}\partial_z A_{3\omega}^2 \simeq -k_0 n_2 A_\omega^3 A_{3\omega}\sin(\Delta\phi). \quad (10)$$

The demand that the spatial profiles of both coupled components remain steady-state in the self-channeling regime suggests $\sin\Delta\phi=0$. Hence, the dephasing $\Delta\phi=3\phi_\omega-\phi_{3\omega}$ should be close to either 0 or π. The fact that only a dephasing of π is possible follows immediately from $\partial_z\Delta\phi\approx 0$: At leading order, $\Delta\phi$ satisfies

$$\partial_z\Delta\phi \simeq \Delta k - \frac{4k_0\rho}{3\rho_c} - 3k_0 n_2[2A_\omega^2 - R(t)] - k_0 n_2 \frac{A_\omega^3}{A_{3\omega}}\cos(\Delta\phi), \quad (11)$$

where one may further approximate the Kerr response $R(t)$ by identifying the time t_{max} for which the temporal dependencies in Eq. (4) are maximum at $z=0$ [43]. For instance, when $t_p=127$ fs, this instant is $t_{max}\simeq 13$ fs and yields $R(t_{max})\simeq 0.83A_\omega^2$, i.e., the effective Kerr index, n_2^{eff}, is equal to $0.83n_2$ in this approximation, so that $2A_\omega^2-R(t)\simeq 1.17A_\omega^2$. Setting $\cos\Delta\phi\approx -1$ ($\Delta\phi\approx\pi$) is then necessary to reach a balance between the mismatch parameter $\Delta k=-5$ cm^{-1} and the nonlinear contributions. At certain instants, Fig. 2(e)

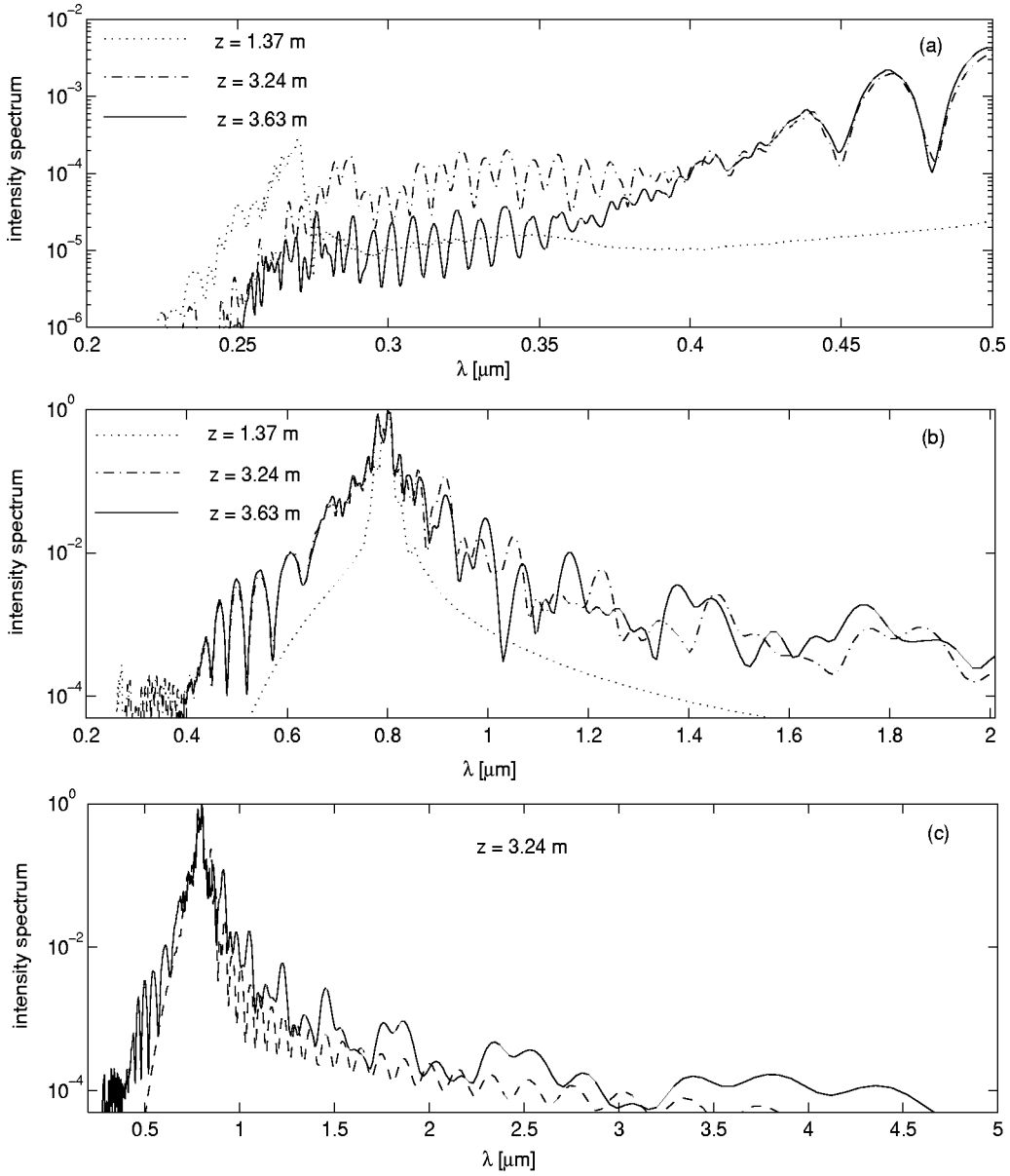

FIG. 3. (a) Intensity spectra up to 500 nm. (b) Same spectra, but extended to 2 μm. (c) Spectra enlarged to 5 μm at $z=3.24$ m with (solid curve) and without (dashed curve) THG.

shows that this balance, however, drops inside short longitudinal intervals. Visual inspection of the numerical results reveals that here either $\mathcal{E}_{3\omega}=0$ or $\mathcal{E}_{\omega}=0$. Such zero-valued components cannot support the previous phase balance. These rapid drops of π-phase shift are responsible for a significant decrease in the energy conversion efficiency [see Fig. 2(f)].

Let us now emphasize one of the most important results of this analysis: The supercontinuum induced by third-harmonic generation.

Figure 3 shows the intensity spectra of the previous pulse. The plotted quantity is the spectral intensity, $\tilde{I}(r,\lambda)$, expressed in Fourier space and integrated over the diffraction plane. Three characteristic stages of pulse broadening in the presence of plasma generation are illustrated. After a Kerr-induced SPM stage (not shown here), a redshift signals the emergence of a leading edge in the pulse temporal profile created by plasma defocusing ($z=1.37$ m). Then, the spectrum is continuously enhanced into a hump of wavelengths in the UV-visible domain ($z=3.24$ m). At larger distances, this hump persists, although the UV components become more damped ($z=3.63$ m). These spectral distortions amplify oscillations mainly caused by constructive/destructive interference between different temporal peaks emerging in the pulse profile and altering consequently the Fourier transform ($\omega_{\mathrm{osc}}\sim 2\pi/\Delta t$, where Δt is the interpeak interval).

These three phases can briefly be explained by the elementary theory for SPM [18], predicting that a Gaussian pulse $\mathcal{E}_{\omega}(L,t)=\mathcal{E}_{\omega}(L_0,t)e^{i\phi(L,t)}$ keeping a nearly constant temporal profile will undergo spectral broadening characterized by a maximum phase shift $\phi_{\max}\sim(I_{\omega}^{\max}/I_0)\times(L/L_{\mathrm{NL}})$, where $L_{\mathrm{NL}}=(k_0 n_2^{\mathrm{eff}} I_0)^{-1}$ is the nonlinear length scale ($L_{\mathrm{NL}}\sim 13$ cm;

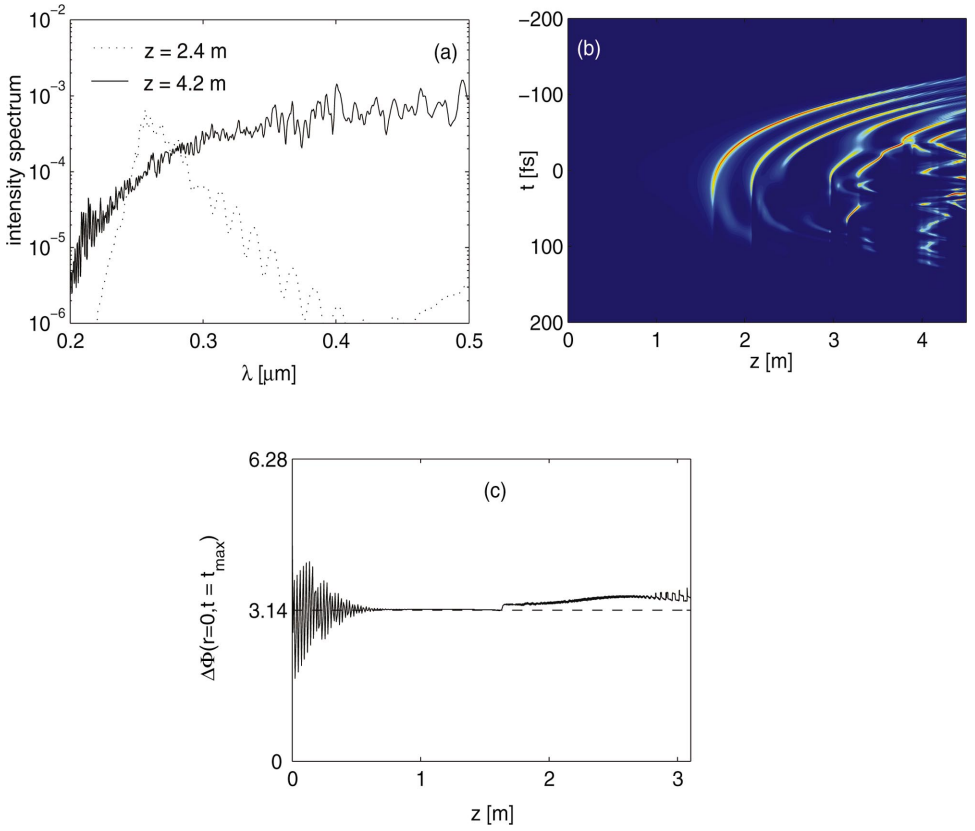

FIG. 4. (Color) (a) Intensity spectra, (b) temporal distribution of the ω component and (c) dephasing of coupled $\omega/3\omega$ pulses formed from a 2.5-mm, high-power ($P_{in}=50\,P_{cr}$) beam.

$I_0=2.6$ TW/cm^2). The frequency variations $\Delta\omega=\omega-\omega_0$ dictating the spectral enlargement are given by $\Delta\omega=-\partial\phi/\partial t$ with maximal value $\Delta\omega_{max}\approx 0.86\phi_{max}/T$, where T is the pulse duration kept quasiconstant along the propagation length L. Applying these estimates to Fig. 3, we find that the competition between Kerr focusing and MPI forms a "constant" leading spike with $T\sim t_p/10$ at $z\sim 1.3$ m, where I_{max} attains 20 times I_0 over the distance $L\sim 0.5$ m. This leads to the frequency broadening $\Delta\omega_{max}\simeq 5\times 10^{15}$ Hz, with a pronounced redshift. Further focusing/defocusing sequences occurring from $z\geqslant 2$ m and achieved by the formation of a central spike close to $t=0$ induce a more symmetric enlargement ($z=3.24$ m). The UV components amplify this spectral dynamics as $\partial_t\phi_{3\omega}\approx 3\partial_t\phi_\omega(\Delta\omega_{3\omega}\approx 3\Delta\omega_\omega)$.

Spectral broadening in wavelength follows the same distortions in the proportion $\Delta\lambda_j=-\lambda_j^2\Delta\omega_j/(2\pi c)$, where c is the speed of light in vacuum. Deviations in wavelengths are found to attain $\Delta\lambda_\omega\simeq 2$ μm for the IR pulse and $\Delta\lambda_{3\omega}=\Delta\lambda_\omega/3\simeq 0.6$ μm for the TH one. At $z=3.24$ m, the deviations $\Delta\lambda_j$ overlap in the region separating the 3ω and ω spectra, which become the locus of an important superimposition of wavelengths. This results in an UV-visible supercontinuum generation in the domain 200 nm$\leqslant\lambda\leqslant$500 nm revealed by Fig. 3(a). Figure 3(b) extends the same spectral evolution, up to 2 μm, while Fig. 3(c) depicts the complete spectrum at $z=3.24$ m with and without THG. From this latter figure, one can conclude that, actually, the hump in wavelength below 500 nm is caused by THG. Moreover, the IR content of the spectrum reaches 4.5 μm, in agreement with experimental observations [20].

B. Broad pulses with high power

To prove that the supercontinuum generation revealed in Fig. 3(a) is generic, we briefly examine the dynamics of a broader Gaussian beam, starting with the input datum (6) having the bigger waist $w_0=2.5$ mm and containing 50 critical powers. The other pulse parameters are kept unchanged. Again, the build-up of UV-visible wavelengths appears over a couple of meters, as displayed by Fig. 4. Figure 4(a) puts in evidence two different stages in the spectral broadening attained at high power levels, for which the nonlinear focus is formed at $z\simeq 1.5$ m. The same "spectral" dynamics characterizes these propagation scales: The TH component widely broadens towards its red direction at $z=2.4$ m, as plasma generation defocuses the back of the pulse. At $z=4.2$ m, a significant "symmetric" enlargement of both pulses results from a distorted temporal distribution mixing leading and trailing peaks. Spectral enlargements strongly superimpose at this distance and promote a salient hump in the wavelength domain 200 nm$\leqslant\lambda\leqslant$500 nm. The temporal evolution of the pulse profile along the z axis can be followed in Fig. 4(b). Over this propagation range, the dephasing $\Delta\phi$ is again clamped around the value π, as seen in Fig. 4(c).

From Fig. 4(b), one can notice how the temporal pulse profiles become distorted at large distances. We must, however, keep in mind that spherically symmetric filaments keeping 50 critical powers during their early propagation are not very realistic, as the focal spot should break up into multiple filaments at powers $\geqslant 20P_{cr}$ [38]. Figure 4 shows, nevertheless, that supercontinuum generation occurs over a few meters in the UV-visible domain, even for broad beams

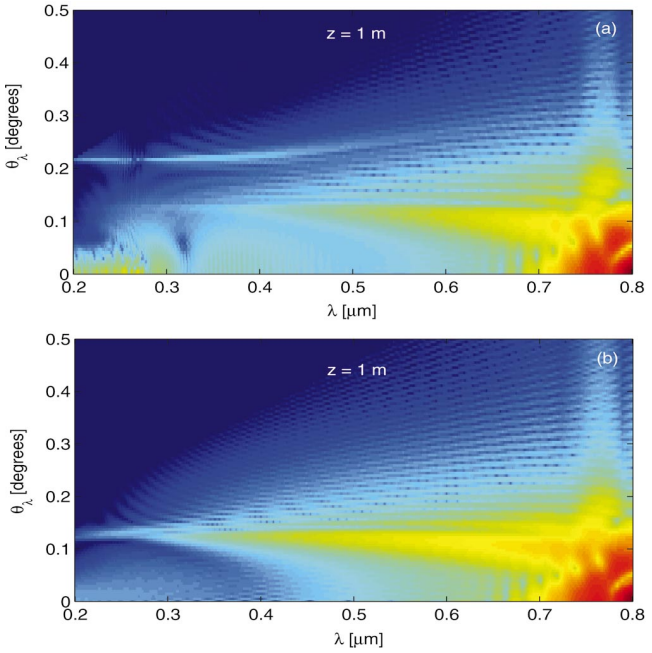

FIG. 5. (Color) Numerically computed CE for the same pulse used in Sec. III, (a) with and (b) without THG, at $z=1$ m.

conveying initially an important ratio of input power over critical.

IV. CONICAL EMISSION

If spectral broadening is linked to the temporal variations of the pulse phase, the conical emission, which manifests as an angular emission of shifted radiation at specific wavelengths, is currently justified by the spatial variations of the same phase. As examined in [19], CE originates from the SPM of an IR pulse. Its half-angle of divergence, θ_λ, is generally measured as the ratio of the radius of a given colored ring to the distance from the middle of the CE source to the screen. This angle does not depend on the longitudinal position where it is measured. Whereas CE has been observed many times for various waists in the range of wavelengths $500\ \text{nm} \leqslant \lambda \leqslant 800\ \text{nm}$ [2,19], little information has been reported for the complementary domain $200\ \text{nm} \leqslant \lambda \leqslant 500\ \text{nm}$.

Since CE originates from the nonlinear phase shifts in one filament, it is worth computing it from the mm-waisted beam ($w_0=0.5$ mm) simulated in Sec. III. For any pulse component, CE follows from the broadening of the angular spectrum defined by $k_\perp=|\partial\phi/\partial r|$, which is mainly driven by the spatial variations of the plasma density ($\sim|\partial\rho/\partial r|$). Along the self-focusing process, radial compression and longitudinal steepening occur simultaneously at the pulse front, which results in a salient increase of the nonlinearities interplaying in the phase [see, e.g., Eq. (7)]. For TH generation, CE is reinforced by the FWM source contribution for the 3ω component. This angular divergence is plotted in Fig. 5 at $z \simeq 1$ m, where the pulse intensity attains its maximum in both components. Figure 5(a) shows the angular divergence computed from the spatio-temporal Fourier spectrum of the total pulse intensity $|\tilde{\mathcal{E}}_\omega(k_\perp,\omega)+\tilde{\mathcal{E}}_{3\omega}(k_\perp,\omega)|^2$, from which the half-angle of propagation at given wavelength λ is $\theta_\lambda \simeq k_\perp/k_z \times (360/2\pi)$ (degrees), where $k_z \simeq 2\pi/\lambda$. For wavelengths above 400 nm, an "inner" bright curve occurs in the plane (θ_λ,λ), which is caused by the fundamental pulse. At smaller wavelengths, a second "outer" curve arises because of the influence of THG. For $\lambda=500$ nm, this angle reaches the value 0.12°, in agreement with available experimental data [2,19]. Figure 5(b) illustrates the CE for the same pulse without THG ($\mathcal{E}_{3\omega}=0$), for which θ_λ slightly increases with decreasing λ, but with an angular growth limited to $\theta_\lambda \sim 0.15°$. In contrast, when TH is generated, CE is noticeably enhanced by about 0.1°. The divergence is steeply augmented to 0.23°–0.25° in the range $200\ \text{nm} \leqslant \lambda \leqslant 400\ \text{nm}$, as the angular contribution from the pump wave becomes more and more extinguished. This angular growth is linked to additional (FWM) nonlinearities coming from the coupling $\omega/3\omega$ ($\partial_r\phi_{3\omega} \approx 3\partial_r\phi_\omega$) and making the TH spectrum in $k_\perp$ wider than the fundamental.

V. EXPERIMENTAL LIDAR SENSING REVEALS UV-VISIBLE SUPERCONTINUUM GENERATION

Since supercontinuum generation in the UV-visible wavelength domain was numerically evidenced over meter-range propagation scales for mm-waisted beams, we may expect to detect the same phenomenon over several hundreds of meters by using cm-waisted pulses. With this aim, experiments were performed by means of the Teramobile laser system [23], delivering pulses with waist w_0 as large as 5 cm from the laser exit.

The Teramobile system is the first mobile femtosecond TW-laser based Lidar system [23]. It involves a chirped pulse amplified (CPA) Ti:sapphire laser source that delivers 5 TW pulses (70 fs, 350 mJ) at 10 Hz repetition rate. The laser pulses are sent vertically into the atmosphere using an all-reflective beam expander ($3\times$). The photons backscattered from the atmosphere are collected by a 40-cm-diam telescope, which focuses the light onto a spectrally resolved detector. The Lidar returns are recorded as a function of the photon flight time using a 500 MHz digital oscilloscope, which provides distance resolution. The initial chirp of the pulse can be modified by varying the grating distance in the compressor, in order to limit the initial optical intensity and to compensate for group-velocity dispersion (GVD) in air as the laser beam propagates. This allows us to modify the distance at which the onset of filamentation occurs.

The UV-visible content of the supercontinuum was measured at different altitudes by using the Lidar arrangement and by scanning the spectrometer. The wavelength increment was 10 nm from 230 nm to 600 nm. For each spectral interval, averaging over 1000 shots was performed. The white light intensity was optimized by changing the initial chirp and geometrical focusing. Optimal white-light emission was found for an initial GVD precompensation chirp of -150 fs ($t_p \simeq 127$ fs) and a linear focusing of $f=10$ m. De-

convolution of the spectral dependence of the apparatus response was applied. Correction over the Rayleigh-Mie backscattering/extinction efficiencies was performed by analyzing the individual Lidar returns. Moreover, correction over the ozone absorption, present in the atmosphere at a concentration of 100 $\mu g/m^3$, was applied to the spectra.

Lidar signals contain information about the intensity profile in a cross section of the beam depending on the altitude [39]. Because of the Lidar optical arrangement, the overlap between the laser beam and the telescope field varies with altitude and strongly depends on the laser divergence. In particular, Lidar signals become very sensitive to this overlap function at low altitude. To correct this function, the whole detection system geometry, including the collecting telescope, the monochromator, and the detector, has been designed in three dimensions in order to calculate the geometrical compression, and hence the overlap function. This function was integrated over the whole beam section. In this integration, following the results of [25], we modeled the laser beam profile at each wavelength as a central emission peak, surrounded by conical emission bearing 70% of the energy. The divergence angle of the conical emission at each wavelength, as well as the laser angle relative to the telescope axis that could not be measured directly, were left as free parameters. These parameters have been determined by fitting the simulated signal as a function of the altitude at each wavelength with the experimental ones. The strongest weight in this fit was given at the lowest altitudes, where the geometrical compression effect is higher, and, therefore, where the signal is more sensitive to the parameters. This fit allowed us to access the white light spectrum at low altitude (100 m–200 m) and the supercontinuum divergence related to conical emission as a function of the wavelength.

The results at 105 m, 135 m, and 195 m altitudes are shown in Fig. 6(a). At 105 m, SPM widely broadens the fundamental laser spectrum and THG appears as a band of some 50 nm around 265 nm. At 135 m, however, the observed spectrum changes into an ultrabroadband and continuous UV-visible plateau down to 230 nm. At 195 m, TH spectral contribution relaxes to some extent, while the hump at visible wavelengths still persists.

This spectral dynamics agrees with the previous numerical results. Some discrepancies, however, deserve special comments. First, experimental and numerical spectra are quite similar, up to the oscillations created by interference between different peaks appearing in the pulse profile (see Fig. 3). Such oscillations are smoothed in the experimental spectra, measured with a resolution of 10 nm, and averaged over 1000 shots. Second, differences also occur in the longitudinal scales. Whereas our numerics emphasizes a spectral dynamics taking place over 2.5 m (see Sec. III), identical spectral distortions develop over several tens of meters in the experiments. We attribute these discrepancies to the large increment ($\simeq$10 m) limiting the number of available experimental data, where the build-up in wavelengths arises as a cumulative effect from all filaments in the entire laser focal spot. A majority of filaments should indeed be aligned on the same spectral profile to modify noticeably the overall laser spectrum, which can happen after several tens of meters along the propagation axis. This conjecture received confirmation in a very recent investigation [44], where UV spectral measurements were performed on a single filament over laboratory scales and restored a supercontinuum similar to Figs. 3(a) and 4(a) over a few meters of propagation only.

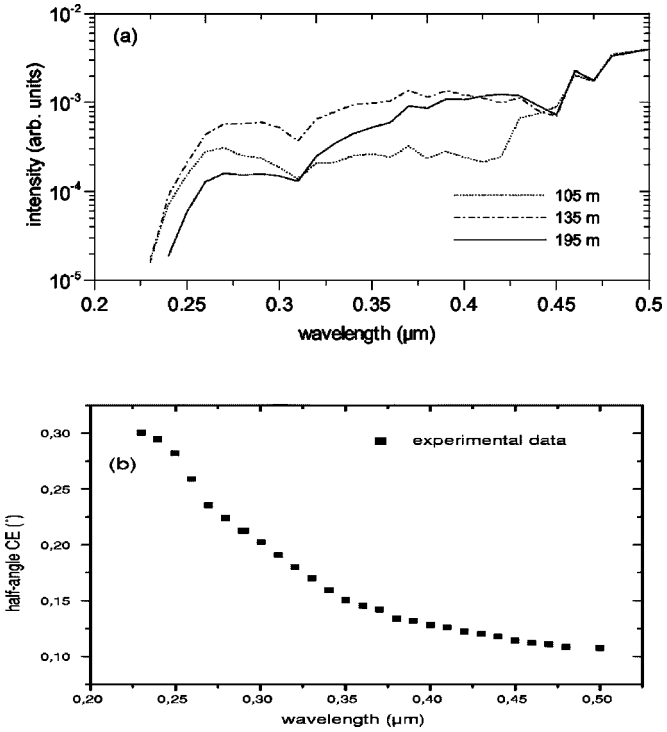

FIG. 6. (a) Spectral evolution measured at different propagation distances. Intensity at 500 nm is fixed at 4×10^{-3} times the intensity in the fundamental [40]. (b) Conical emission experimentally reported at 200 m altitude for $\lambda<500$ nm.

Figure 6(b) shows the conical emission detected from the same experimental setup. The observed divergence can be explained as the convolution of CE from each filament in the bundle (overall beam) and the linear divergence of the Teramobile bundle itself [25]. This latter angle corresponds to the whole beam divergence governed by geometrical optics, due to the 10-m focusing geometry. It is determined by subtracting the CE angles known from the literature in the domain of 500–600 nm from the global divergence of the beam. The resulting value is then used to deduce the CE angles at lower wavelengths, which are presented in Fig. 6(b) (squares). Basically, the conical emission in the UV-visible wavelength domain prolongs almost linearly that known from IR pulses at relatively larger wavelengths [19]. This behavior is true, up to an important deviation of the half-angle θ_λ at UV wavelengths $\lambda<350$ nm. This deviation increases the CE by more than 0.1° and reaches 0.28° at 250 nm, which reasonably agrees with the simulations of Sec. IV.

Note that, whereas IR and UV components are connected in Fig. 6(b), they look disconnected in Fig. 5(a). We believe that this discrepancy originates from the lack of higher-order dispersion and space-time focusing terms in our model equations. These effects are indeed awaited to match the two spectral components by increasing their own angular divergence (see, e.g., Ref. [45]).

VI. THG IS A NONLINEAR SATURATION MECHANISM FOR THE PUMP WAVE

As revealed by Fig. 1(d), THG enables the two-colored filament to propagate further by keeping a quasiconstant waist of ~ 100 μm. This phenomenon is compatible with the weaker energy loss undergone by the filament when TH is emitted, compared with the propagation of an IR pulse alone [Fig. 1(f)]. By computing the continuity relations for the wave densities, Eqs. (9) and (10) indeed show that generation of third harmonics takes place by FWM through up- and down-conversion cycles, which, on the whole, do not affect the global energy content. Converting part of the fundamental energy into TH thus limits the energy loss undergone by plasma formation.

To understand the self-channeling enhancement, we can first notice the order of magnitude of the wave-vector mismatch parameter: $|\Delta k| = 5$ cm^{-1}. This parameter is large compared with the typical "nonlinear wave vector" associated with the peak intensity of the ω component: $n_2 k_0 A_\omega^2 < 2.5$ cm^{-1}. More precisely, $|\Delta k|$ has an order of magnitude comparable with the XPM and FWM contributions of Eq. (3), so that we can apply the so-called "cascading" limit which consists in setting Δk equal to the leading-order nonlinearities, i.e.,

$$\mathcal{E}_{3\omega} \simeq -\frac{k_0 n_2}{|\Delta k| + 6k_0 n_2 A_\omega^2} \mathcal{E}_\omega^3. \tag{12}$$

As long as $A_\omega^2 < |\Delta k|/6k_0 n_2 = 2.7 \times 10^{13}$ W/cm^2, the approximation $\mathcal{E}_{3\omega} \approx -k_0 n_2 \mathcal{E}_\omega^3/|\Delta k|$ holds. Once Eq. (12) is plugged into the pump wave equation, Eq. (2) simplifies at leading order into

$$\begin{aligned} \partial_z \mathcal{E}_\omega \simeq & \frac{i}{2k_0} \nabla_\perp^2 \mathcal{E}_\omega - \frac{i}{2} k_\omega'' \partial_t^2 \mathcal{E}_\omega + i k_0 n_2 R(t) \mathcal{E}_\omega \\ & - i\left(\frac{k_0}{2\rho_c} - i\frac{\sigma_\omega}{2} \right) \rho \mathcal{E}_\omega - \frac{\beta_\omega^{(K_\omega)}}{2} |\mathcal{E}_\omega|^{2K_\omega - 2} \mathcal{E}_\omega \\ & - i k_0 n_2 \left[\frac{k_0 n_2}{|\Delta k|} \right] \frac{|\mathcal{E}_\omega|^4}{(1 + C|\mathcal{E}_\omega|^2)} \mathcal{E}_\omega, \end{aligned} \tag{13}$$

where $C \equiv 6k_0 n_2/|\Delta k|$. The TH nonlinearities thus combine into a defocusing quintic saturation, which becomes itself saturated at high enough intensities ($I_\omega \to I_\omega^{\max}$). Therefore, THG acts in the sense of "delaying" the collapse of the pump wave and stabilizes the self-guided filament to some extent. A similar phenomenon was earlier discovered in [41] for cw beams without plasma generation: At large, negative mismatch values $\Delta k/(n_2 k_0 A_\omega^2) < -1$, THG promoted the arrest of beam collapse and contributed to form $\chi^{(5)}$-like spatial solitons ($C \to 0$) characterized by periodic oscillations. Such oscillations, which anticipate the convergence of nonlinear beams to solitary-wave structures over long ranges [42], are visible in Figs. 1(c) and 1(d) from $z = 1$ m. In the present context, they decrease in amplitude until MPA dissipates the filament.

Let us estimate the intensity threshold for the ω component resulting from the interplay between MPI and Kerr focusing. The order of magnitude of the laser intensity, $I_\omega \equiv |\mathcal{E}_\omega|^2$, when it becomes saturated by MPI takes the value $I_{\omega,MPI}^{\max} \simeq (2\rho_c n_2^{\text{eff}}/t_p \sigma_{(K_\omega)} \rho_{\text{nt}})^{1/(K_\omega - 1)} \simeq 48$ TW/cm^2, where $n_2^{\text{eff}} \simeq 0.83 n_2$. In the absence of THG, the typical length for self-channeling is then given by

$$\Delta z_{\text{MPA}} \sim \frac{2}{\beta_\omega^{(K_\omega)} (I_{\omega,MPI}^{\max})^{K_\omega - 1}} \approx 1.1 \text{ m}. \tag{14}$$

If we now consider the role of TH in the limit $C \to 0$, the third harmonics couples with the fundamental like an effective $\chi^{(5)}$ nonlinearity [4] with related coefficient n_4,

$$n_4 = \frac{n_2^2 k_0}{|\Delta k|} \simeq 2.513 \times 10^{-33} \text{ cm}^4/\text{W}^2, \tag{15}$$

which is about a quarter of the value often proposed in the literature (see, e.g., [4]). In spite of the smallness of n_4, one can see that such quintic nonlinearities are active in stabilizing the filament for the following reason.

When we analyze the effective nonlinear index of refraction associated with Eq. (13), i.e.,

$$\begin{aligned} \Delta n &= n_2 R(t) - n_4 |\mathcal{E}_\omega|^4 - \rho_{\max}/2\rho_c \\ &\simeq n_2^{\text{eff}} I_\omega - n_4 I_\omega^2 - \frac{t_p \sigma_{(8)} \rho_{\text{nt}}}{2\rho_c} I_\omega^{K_\omega}, \end{aligned} \tag{16}$$

the combination of nonlinearities can be rewritten as

$$\Delta n = n_2^{\text{eff}} I_{\omega,MPI}^{\max} y (1 - y^{K_\omega - 1} - \alpha y). \tag{17}$$

Here, $y \equiv I_\omega / I_{\omega,MPI}^{\max}$ and $\alpha = I_{\omega,MPI}^{\max}/I_{\omega,\chi^{(5)}}^{\text{th}}$ involves the saturation threshold owing to TH-induced quintic saturation,

$$I_{\omega,\chi^{(5)}}^{\text{th}} = \frac{n_2^{\text{eff}}}{n_4} = 1.32 \times 10^{14} \text{ W/cm}^2. \tag{18}$$

Even higher than $I_{\omega,MPI}^{\max}$, quintic saturation still plays a significant role in lowering the overall intensity threshold. Computing the zeros of Δn, for which MPI and $\chi^{(5)}$ nonlinearities both saturate Kerr focusing, no longer yields the solution $y = 1$, but instead $y = 0.94$, which lowers $I_\omega^{\max}$ below 4.5×10^{13} W/cm^2. The self-guiding length is then enhanced accordingly,

$$\Delta z_{\text{MPA}} \sim \frac{2}{\beta_\omega^{(K_\omega)} (I_{\omega,MPI}^{\max} y)^{K_\omega - 1}} \approx 1.63 \text{ m}. \tag{19}$$

It becomes augmented by the multiplicative factor $y^{-7} \sim 1.5$, which agrees with Fig. 1(d).

Figure 7 shows the peak intensity [7(a)], mean beam radius [7(b)], temporal distribution [7(c)], and averaged spectra at $z = 3.24$ m [7(d)] from the input beam (6) used as an initial condition for Eq. (13). In Figs. 7(a) and 7(b), the dashed lines report the peak intensity and mean radius plotted in Fig. 1(a), while the dotted curve represents the same quantities computed from Eq. (13) in the pure $\chi^{(5)}$ limit, $C \to 0$. Remarkably, this equation restores nearly the same pulse dynamics as that observed in Figs. 1(a), 1(b), and 3(c). Even though THG is "formally" not existing in Eq. (13), its corresponding quintic saturation promotes close temporal distortions [Fig. 7(c)]. It helps in symmetrizing the pulse spectra and in enhancing spectral enlargement towards the blue side,

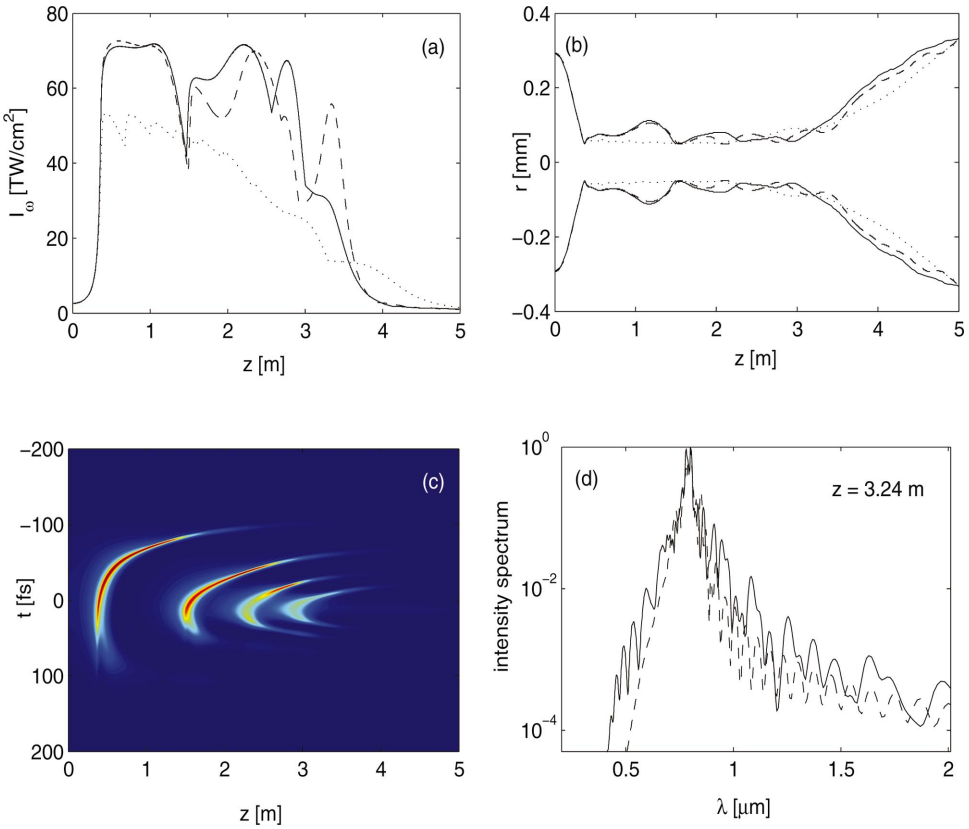

FIG. 7. (Color) (a) Peak intensities for a 0.5 mm-waisted pulse with $4P_{cr}$ taken as the input condition for Eq. (13) (solid curve), for Eqs. (2) and (3) (dashed curve) and in the pure $\chi^{(5)}$ limit $C \to 0$ (dotted curve). (b) Mean FWHM radius of the same solutions. (c) Temporal distribution corresponding to the dynamics described by Eq. (13). (d) Averaged spectrum at $z = 3.24$ m computed from Eq. (13) (solid curve) and from Eq. (2) without THG (dashed curve).

compared with an IR pulse undergoing plasma defocusing alone [Fig. 7(d)]. These last numerical results reproduce spectra resembling those depicted in Fig. 3, apart from the UV broadband earlier excited by THG which is, of course, absent here. They suggest that, even if current models of pulses propagating in air may not account for TH excitation and discard integration of Eq. (3), they should at least include a saturated quintic nonlinearity [last term in Eq. (13)] with the effective n_4 given by Eq. (15).

VII. CONCLUSION

In summary, we have investigated the influence of phase-locked propagation of TH pulses on the white-light continuum spectrum generated by the fundamental IR pulse over meter-range propagation distances. From numerical computations supported by theoretical estimates, we demonstrated that the third-order harmonics significantly contributes to the supercontinuum generation. As already expected in [29,30], TH is generated and maintains the beam energy and intensity over long distances within a two-colored filament. In this filament, the IR pulse is subject to SPM which broadens the spectrum asymmetrically towards the red direction, caused by the early plasma defocusing of the back of the pulse. Simultaneously, the UV spectral region undergoes a wide broadening, as the dephasing between the two components stays locked at $\Delta\phi = \pi$ all along the self-channeling process. This property, discovered in [29] over a few cm, has been put in evidence upon several meters of filamentation. The π-phase locking guarantees that SPM of the dominant IR pulse has a direct incidence on the UV part in the spectrum, which becomes three times more enlarged in frequency. This mechanism finally results in a superimposition of the blue-shifted IR spectrum with the strongly redshifted UV one and to the build-up of novel wavelengths in the intermediate range 200 nm $\leqslant \lambda \leqslant$ 500 nm. This phenomenon was experimentally confirmed by atmospheric sensing experiments performed with the Teramobile laser facility. By means of chirped (150 fs), cm-waisted pulses delivering several TW in power, vertical shots in the atmosphere allowed us to display evidence of this supercontinuum generation starting from the deepest UV wavelengths.

Next, we analyzed the conical emission induced by the spatial variations occurring in the nonlinear phase of the two-colored filament. Numerical computations of the CE revealed that the angular divergence still increases at decreasing wavelengths going down to the UV region, in the same proportions as inside the Teramobile bundle. A steep angular deviation of 0.1° produced at $\lambda \sim 250$ nm was revealed by both the experiment and numerical computations, which clearly proves that the TH component undergoes a more important spectral diffraction. Increase of the CE angle at UV wavelengths is also a consequence of the π-phase locking. It can also be attributed to the additional saturable nonlinearity originating from THG, which reinforces the defocusing action of MPI.

In connection with this point, the last—but not least—important result consisted in the partial stabilization of the two-colored filament by THG, whose principal effect on the IR pulse dynamics is to introduce a quintic, defocusing nonlinearity at large wave-vector mismatch values. This extra defocusing contribution arises as a saturating nonlinearity in

the form $-n_4|\mathcal{E}_\omega|^4\mathcal{E}_\omega/(1+6k_0n_2|\mathcal{E}_\omega|^2/|\Delta k|)$, which lowers the maximum intensity threshold reached by the ω component and, thereby, enhances the self-guiding range by an efficient decrease of the MPA damping of the filament. Even weak, this stabilization mechanism participates in making SPM-broadened spectra more symmetric and prolonging the lifetime of the filament.

The question of knowing whether $\chi^{(5)}$ saturation is important or not was raised in several recent papers (see, e.g., [4,5]), where quintic saturations were suggested to influence the propagation dynamics. However, no precise evaluation of the quintic coefficient n_4 was given, as no specific measurement of higher-order nonlinearities was realized nowadays at 800 nm for di-oxygen molecules. Our present investigation clearly shows that THG can be a key player in stabilizing femtosecond filaments in air by acting like a $\chi^{(5)}$ defocusing nonlinearity with a quite definite n_4 coefficient proposed in Eq. (15). Further models of femtosecond pulse propagation in air should be modified accordingly.

ACKNOWLEDGMENTS

The authors thank Professor Falk Lederer and Professor Ulf Peschel for fruitful discussion. Experiments were realized in the framework of the Teramobile Project, funded jointly by CNRS and DFG.

[1] A. Braun, G. Korn, X. Liu, D. Du, J. Squier, and G. Mourou, Opt. Lett. **20**, 73 (1995).
[2] E. T. J. Nibbering, P. F. Curley, G. Grillon, B. S. Prade, M. A. Franco, F. Salin, and A. Mysyrowicz, Opt. Lett. **21**, 62 (1996).
[3] B. LaFontaine, F. Vidal, Z. Jiang, C. Y. Chien, D. Comtois, A. Desparois, T. W. Johnston, J. C. Kieffer, H. Pépin, and H. P. Mercure, Phys. Plasmas **6**, 1615 (1999).
[4] N. Aközbek, C. M. Bowden, A. Talebpour, and S. L. Chin, Phys. Rev. E **61**, 4540 (2000).
[5] N. Aközbek, M. Scalora, C. M. Bowden, and S. L. Chin, Opt. Commun. **191**, 353 (2001).
[6] I. G. Koprinkov, A. Suda, P. Wang, and K. Midorikawa, Phys. Rev. Lett. **84**, 3847 (2000).
[7] H. R. Lange, G. Grillon, J. F. Ripoche, M. A. Franco, B. Lamouroux, B. S. Prade, A. Mysyrowicz, E. T. J. Nibbering, and A. Chiron, Opt. Lett. **23**, 120 (1998).
[8] A. Brodeur, C. Y. Chien, F. A. Ilkov, S. L. Chin, O. G. Kosareva, and V. P. Kandidov, Opt. Lett. **22**, 304 (1997).
[9] M. Mlejnek, E. M. Wright, and J. V. Moloney, Opt. Lett. **23**, 382 (1998).
[10] S. Champeaux and L. Bergé, Phys. Rev. E **68**, 066603 (2003).
[11] J. Schwarz, P. Rambo, J. C. Diels, M. Kolesik, E. M. Wright, and J. V. Moloney, Opt. Commun. **180**, 383 (2000).
[12] S. Tzortzakis, B. Lamouroux, A. Chiron, M. Franco, B. Prade, A. Mysyrowicz, and S. D. Moustaizis, Opt. Lett. **25**, 1270 (2000).
[13] A. Couairon and L. Bergé, Phys. Rev. Lett. **88**, 135003 (2002).
[14] A. Couairon, S. Tzortzakis, L. Bergé, M. Franco, B. Prade, and A. Mysyrowicz, J. Opt. Soc. Am. B **19**, 1117 (2002).
[15] Th. Lehner and N. Auby, Phys. Rev. E **61**, 1996 (2000).
[16] H. Ward and L. Bergé, Phys. Rev. Lett. **90**, 053901 (2003).
[17] A. L. Gaeta, Phys. Rev. Lett. **84**, 3582 (2000).
[18] G. P. Agrawal, *Nonlinear Fiber Optics*, 3rd ed. (Academic, New York, 2001), pp. 274.
[19] O. Kosareva, V. P. Kandidov, A. Brodeur, C. Y. Chien, and S. L. Chin, Opt. Lett. **22**, 1332 (1997).
[20] J. Kasparian, R. Sauerbrey, D. Mondelain, S. Niedermeier, J. Yu, J. P. Wolf, Y. B. André, M. Franco, B. Prade, S. Tzortzakis, A. Mysyrowicz, M. Rodriguez, H. Wille, and L. Wöste, Opt. Lett. **25**, 1397 (2000).
[21] L. Wöste, C. Wedekind, H. Wille, P. Rairoux, B. Stein, S. Nikolov, C. Werner, S. Niedermeier, F. Ronneberger, H. Schillinger, and R. Sauerbrey, Laser Optoelektron. **29**, 51 (1997).
[22] S. L. Chin, S. Petit, F. Borne, and K. Miyazaki, Jpn. J. Appl. Phys., Part 2 **38**, L126 (1999).
[23] H. Wille, M. Rodriguez, J. Kasparian, D. Mondelain, J. Yu, A. Mysyrowicz, R. Sauerbrey, J. P. Wolf, and L. Wöste, Eur. Phys. J.: Appl. Phys. **20**, 183 (2002).
[24] J. Kasparian, M. Rodriguez, G. Méjean, J. Yu, E. Salmon, H. Wille, R. Bourayou, S. Frey, Y. B. André, A. Mysyrowicz, R. Sauerbrey, J. P. Wolf, and L. Wöste, Science **301**, 61 (2003).
[25] M. Rodriguez, R. Bourayou, G. Méjean, J. Kasparian, J. Yu, E. Salmon, A. Scholz, B. Stecklum, J. Eislöffel, U. Laux, A. P. Hatzes, R. Sauerbrey, L. Wöste, and J. P. Wolf, Phys. Rev. E **69**, 036607 (2004).
[26] G. Méjean, J. Kasparian, E. Salmon, J. Yu, J. P. Wolf, R. Bourayou, R. Sauerbrey, M. Rodriguez, L. Wöste, H. Lehmann, B. Stecklum, U. Laux, J. Eislöffel, A. Scholz, and A. P. Hatzes, Appl. Phys. B: Lasers Opt. **77**, 357 (2003).
[27] J. P. Wolf, *Encyclopedia of Analytical Chemistry*, edited by R. A. Meyers (Wiley, Chichester, 2000), Vol. 3, pp. 2226–2245.
[28] G. Méjean, J. Kasparian, J. Yu, S. Frey, E. Salmon, and J. P. Wolf, Appl. Phys. B: Lasers Opt. **78**, 535 (2004).
[29] N. Aközbek, A. Iwasaki, A. Becker, M. Scalora, S. L. Chin, and C. M. Bowden, Phys. Rev. Lett. **89**, 143901 (2002).
[30] H. Yang, J. Zhang, J. Zhang, L. Z. Zhao, Y. J. Li, H. Teng, Y. T. Li, Z. H. Wang, Z. L. Chen, Z. Y. Wei, J. X. Ma, W. Yu, and Z. M. Sheng, Phys. Rev. E **67**, 015401(R) (2003).
[31] Y. R. Shen, *The Principles of Nonlinear Optics* (Wiley, New York, 1984).
[32] S. Backus, J. Peatross, Z. Zeek, A. Rundquist, G. Taft, M. M. Murnane, and H. C. Kapteyn, Opt. Lett. **21**, 665 (1996).
[33] A. B. Fedotov, N. I. Koroteev, M. M. T. Loy, X. Xiao, and A. M. Zheltikov, Opt. Commun. **133**, 587 (1997).
[34] G. Marcus, A. Zigler, and Z. Henis, J. Opt. Soc. Am. B **16**, 792 (1999).
[35] C. J. Zhu, Y. D. Qin, H. Yang, S. F. Wang, and Q. H. Gong, Chin. Phys. Lett. **18**, 57 (2001).
[36] J. F. Ripoche, G. Grillon, B. Prade, M. Franco, E. Nibbering, R. Lange, and A. Mysyrowicz, Opt. Commun. **135**, 310 (1997).
[37] L. Bergé and A. Couairon, Phys. Plasmas **7**, 210 (2000).
[38] L. Bergé, S. Skupin, F. Lederer, G. Méjean, J. Yu, J. Kaspar-

ian, E. Salmon, J. P. Wolf, M. Rodriguez, L. Wöste, R. Bourayou, and R. Sauerbrey, Phys. Rev. Lett. **92**, 225002 (2004); S. Skupin, L. Bergé, U. Peschel, F. Lederer, G. Méjean, J. Yu, J. Kasparian, E. Salmon, J. P. Wolf, M. Rodriguez, L. Wöste, R. Bourayou, and R. Sauerbrey, Phys. Rev. E **70**, 046602 (2004).

[39] R. M. Measures, *Laser Remote Sensing—Fundamentals and Applications* (Wiley Interscience, New York, 1984).

[40] P. Rairoux, H. Schillinger, S. Niedermeier, M. Rodriguez, F. Ronneberger, R. Sauerbrey, B. Stein, D. Waite, C. Wedekind, H. Wille, L. Wöste, and C. Ziener, Appl. Phys. B: Lasers Opt. **71**, 573 (2000).

[41] A. V. Buryak, V. V. Steblina, and R. A. Sammut, Opt. Lett. **24**, 1859 (1999).

[42] L. Bergé, Cl. Gouédard, J. Schjødt-Eriksen, and H. Ward, Physica D **176**, 181 (2003).

[43] L. Bergé, Phys. Rev. E **69**, 065601(R) (2004).

[44] G. Méjean, J. Kasparian, J. Yu, S. Frey, E. Salmon, R. Ackermann, J. P. Wolf, L. Bergé, and S. Skupin (unpublished).

[45] M. Kolesik, G. Katona, J. V. Moloney, and E. M. Wright, Phys. Rev. Lett. **91**, 043905 (2003); M. Kolesik, E. M. Wright, and J. V. Moloney, *ibid.* **92**, 253901 (2004).